# An Elastohydrodynamic Lubrication (EHL) Model for Radial Piston Motors

Jinhwan Lee[1], Lizhi Shang[1], and Pierre BERNARD[2]

[1]Maha Fluid Power Research Center, Purdue University, Lafayette, IN, USA
E-mail: lee4775@purdue.edu, shangl@purdue.edu
[2] Poclain Hydraulics Industrie, Verberie, France
E-mail: pierre.bernard@poclain.com

## Abstract

This study presents an Elastohydrodynamic Lubrication (EHL) simulation model developed for a multi-lobe radial piston motor and its experimental validation. Since those types of radial piston motors are frequently operated under high torque and low-speed conditions, the severe wear and excessive power loss challenge their lubricating interface design. However, understanding these lubrication interfaces has been limited by difficulties in experimental measurement under high pressure in small gaps and the complexity of the multi-physics involved. To address these challenges, the proposed model solves a density-based Reynolds equation to predict tribological behaviors of fluid films around a stepped piston with the consideration of multi-body dynamics, port and throttling loss, and elastic deformations. The simulation results indicate that the lubrication regimes and asperity contact pressure strongly rely on the chamber pressure and motor rotational speed. The roller – bushing interface undergoes mixed lubrication regimes, and severe asperity contact occurs in piston – cylinder interfaces, indicating boundary lubrication during high load conditions. In addition, the interaction between the fluid films demonstrated an asymmetric deformation of the piston, significantly influencing the hydrodynamic pressure and film thickness distributions in the roller – bushing interface. Also, the consideration of tilting of a piston was essential to predict hydrodynamic and asperity contact pressures for piston – cylinder interfaces. As a result, the power loss analysis identified the main power loss contributors; the upper piston – cylinder interface, and throttling loss. This paper presents the simulation, the governing equations, the numerical solver, the force balance calculation, and the fluid and structure interactive scheme. The paper also compares the simulated friction torque and contact area against the experimental measurement. The developed model can provide insights into fluid film behaviors and assess the effect of design parameters such as clearance, dimensions, and material properties on tribological characteristics of radial piston motors.

**Keywords**: Radial piston motors, elastohydrodynamic lubrication, deformation, power loss.

## 1 Introduction

A multi-lobe radial piston motor is essential in various industrial applications that require high-torque actuation, especially a hydraulic transmission in mobile hydraulics for construction and agricultural machinery. Radial piston motors convert the flow energy from pressurized inlet fluid into mechanical work through the movement of pistons. In this process, forces are transferred through a series of components—cam, roller, bushing, piston, and cylinder bore wall—via lubricating interfaces. The hydrostatic pressure applied to the piston is balanced by the normal force from the cam, causing the piston to exert force on the cylinder wall and generate torque. More details on the working principle of radial piston motors can be found in [1,2].

Tribological behaviors of the lubricating interfaces can substantially affect the overall efficiency and reliability of radial piston motors. There are multiple lubricating interfaces for a typical stepped piston assembly as described in fig. 1. The cam – roller interface is a nonconformal rolling contact, and the roller – bushing interface is a conformal contact. Also, the connected upper and separate lower bore interfaces are piston – cylinder interfaces that do not have reliable pressure build-up mechanisms. Radial piston motors typically operate at low speeds and high loads, and these operating conditions have the potential to result in excessive power loss due to increased solid friction from asperity contact and mechanical failure from surface damage.

Many experimental research works focused on improving the overall performance of the lubricating interfaces by reducing frictional coefficient and surface damage. Olsson et al [1] used a simulated test bench to investigate the effect of lubricant properties on tribological behaviors of a piston – cylinder interface, assuming a rectangular contact area. Pettersson et al [3] showed that the textured surfaces of a roller – piston interface could improve friction coefficient variation. Lewis [4] studied the effect of surface layer material on

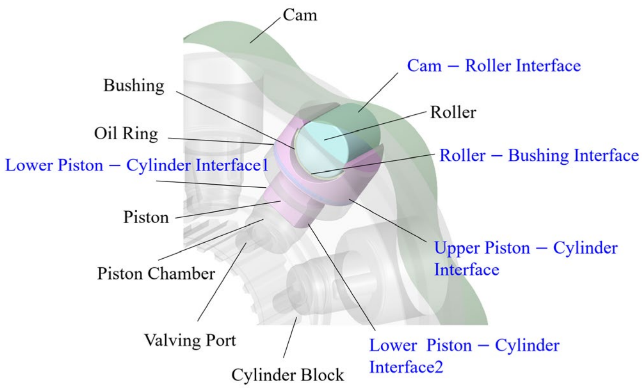


*Figure 1: Lubricating Interfaces.*

friction coefficient and scuffing damage with different lubricant supply conditions and demonstrated lower friction coefficient with cloth material than sintered bronze. Nilsson et al [5] studied seizure mechanisms of a radial piston motor under actual motor operation conditions using a test configuration that can measure hydromechanical losses. They demonstrated that seizure could initiate from a roller – piston interface and piston – cylinder interface with increased hydromechanical loss, severe wear, and scuffing. A drawback with the above-mentioned works is that their results may not exactly represent the motor operation condition because the lubricating interfaces were investigated in isolation with simplified test setups in which lubricating conditions might be different [1,3,4]. Also, experimental studies may need bulky and high-cost test rigs that cannot be easily configurable for different machine designs. Above all, it is difficult to directly measure important physical quantities such as hydrodynamic pressure, asperity contact pressure, and film thickness. To address those difficulties, many numerical models were proposed to understand the behaviors of lubricating interfaces in hydraulic machines. Dahlén et al [6] proposed a full film lubrication model for the roller – bushing interface and valving interface in a radial piston motor by solving a Reynolds equation. Isaksson et al [7, 8] proposed a full film and mixed lubrication model for the roller – piston interface with a hydrostatic groove, considering the piston deformation and surface roughness. Zhang et al [9] proposed the unsteady EHL model for a roller – piston interface and showed a slotted hole could largely increase the film thickness. Zhang et al [10] proposed a modified lubrication model for a roller – piston interface with a focus on thermal analysis, demonstrating a significant temperature rise from viscous and asperity friction. Li et al [11] proposed a CFD simulation for a valving interface with leakages and volumetric efficiency analysis. Besides simulation models for radial piston motors, more advanced coupled simulation models have been developed for other types of hydraulic machines. Ransegnola et al [12] proposed a simulation model that considered multiple lubricating interfaces in a swashplate-type axial piston machine to investigate piston and slipper spin. Mukherjee et al [13] developed a coupled thermal simulation model to study the effect of thermal behaviors on the efficiency and film thickness in a swashplate-type axial piston machine. However, a coupled EHL simulation model for a radial piston motor that considers various multiphysics such as transient chamber pressure, lubricating interfaces, asperity contact, rigid body dynamics, and deformation has never been developed. Also, previous numerical studies for a radial piston motor neglected the piston dynamics in the actual operations such as tilting which greatly affected the asperity contact pressure and area in this work. Moreover, the interaction between the roller – bushing interface and piston – cylinder interface has never been accounted for due to complexity despite their combined significant effect on the deformation and dynamics of the piston. This explains why although a considerable amount of experimental work and simulation models have been made for the lubricating interfaces in radial piston motors, designing those lubricating interfaces remains a challenge for engineers with a limited understanding of their behaviors.

The purpose of this study is to develop and validate a coupled EHL simulation model that can assess various design

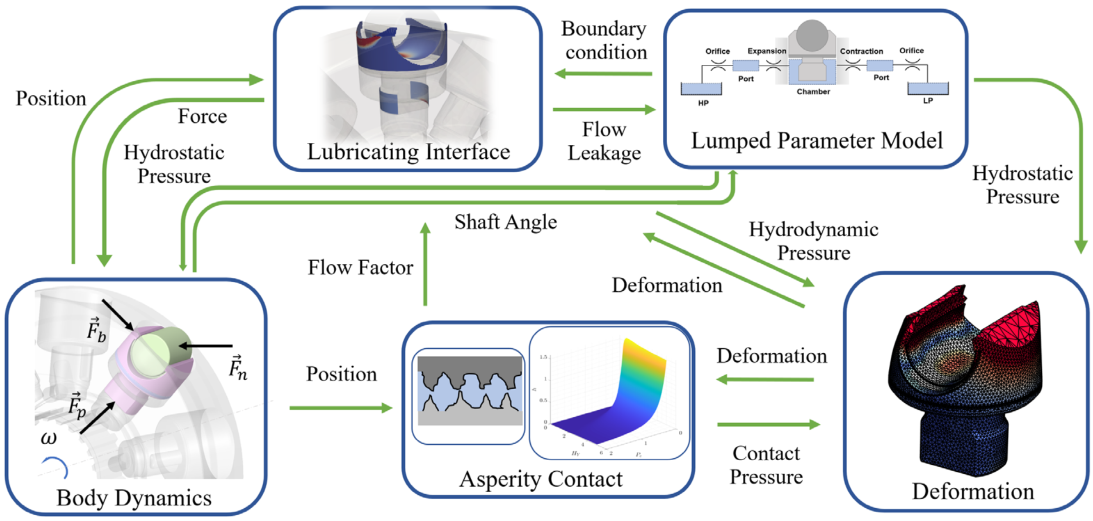


*Figure 2: Simulation domains.*

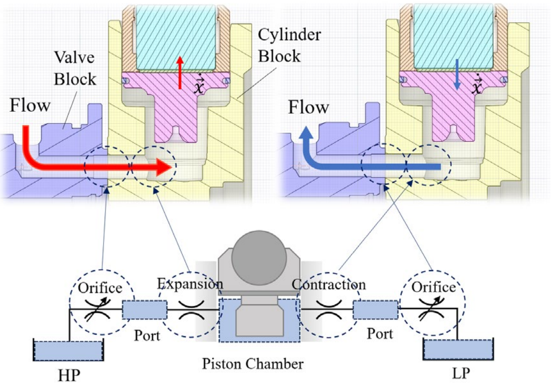


*Figure 3: Hydraulic circuit for the LP model.*

parameters and provide physical insights into tribological behavior considering actual motor operation. Universal Reynolds equations for the roller – piston interface and piston – cylinder interfaces are fully coupled with the lumped parameter model, rigid body dynamics, and deformation caused by hydrodynamic and asperity contact pressures. The physical quantities exchanged between different physical domains are illustrated in fig. 2. In an effort to validate the developed simulation model, experimental measurement was performed for the roller – bushing interface, and all lubricating interfaces including piston – cylinder interface. A commercially available MSE08 from Poclain Hydraulics Industrie with a maximum displacement of 1248 cc and power of 41 kW was chosen as a reference machine. The working fluid is ISO VG46 and an isothermal condition of 50 °C is considered for typical operating conditions of the machine. The simulation was run for the shaft speed ranging from 30 RPM to 80 RPM, inlet pressure ranging from 50 bar to 350 bar, and outlet pressure set to 20 bar.

## 2 Numerical models

### 2.1 Lumped parameter (LP) model

The LP model is crucial to the entire simulation because it calculates the piston chamber pressure, which other domain solvers rely on, and the throttling loss, another major source of the power losses. The cross-section view of a piston with the

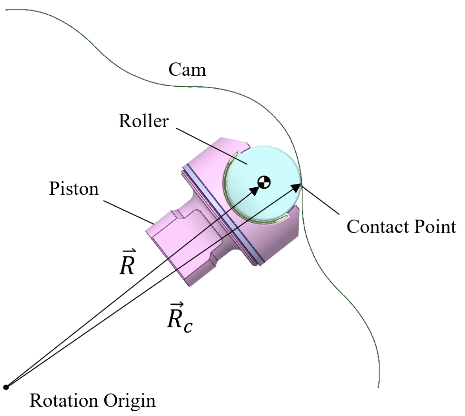


*Figure 4: Piston and roller kinematics.*

valving interface and its equivalent hydraulic circuit are presented in fig. 3. As the cylinder block rotates, the port is alternatively connected to the high-pressure inlet and low-pressure outlet. When the port connects to the high-pressure inlet, the piston moves upward, increasing the piston chamber volume; when it connects to the low-pressure outlet, the piston moves downward. The port connection is where the throttling loss occurs, and any flow leakage or friction loss through the valving interface was not considered in the simulation.

While computationally cost effective and reasonably accurate model to calculate pressure for a control volume such as a piston chamber and port is pressure build-up equation (eq. (1)) where $p$, Κ and $V$ represent volume averaged pressure, isothermal bulk modulus, and chamber volume.

$$\frac{dp}{dt} = \frac{\mathrm{K}}{V}\left(\sum Q - \frac{dV}{dt}\right) \tag{1}$$

Also, the volume flow $Q$ in eq. (1) depends on opening area $A$ of the valving port and the pressure difference $\Delta p$, and this can be modeled as flow with a restrictive orifice (eq. (2)). $C_f$ and $\rho$ represent orifice discharge constant and averaged density of the fluid.

$$Q = C_f A \sqrt{\frac{2\Delta p}{\rho}} \tag{2}$$

In addition to the throttling loss, expansion and contraction of the flow path may provide additional pressure drop, $\Delta p$ as modeled in eq. (3). $\kappa$ and $f$, $L$, $D$, and $v$ represent minor loss coefficient, Darcy friction coefficient, port length, port diameter, and averaged flow velocity respectively.

$$\Delta p = \left(\kappa + f\frac{L}{D}\right)\frac{\rho v^2}{2} \tag{3}$$

Since the orifice opening area and volume change are function of a motor shaft angle, eq (1), (2) and (3) should be solved simultaneously with body dynamics.

### 2.2 Lubricating interface

The hydrodynamic pressure of the lubricating interfaces can be calculated using the density-based universal Reynolds equation for a mixed lubrication suggested by Ransegnola [14] where $\phi_P$, $\phi_S$, $\phi_C$ and $\phi_R$ represents pressure flow factor, shear flow factor, contact flow factor, and roughness flow factor in eq (4). The equation considers the effect of asperity contact on hydrodynamic pressure by introducing the concept of averaged flow using flow factors. The pressure flow factor $\phi_P$ represents increased resistance from asperity for pressure-driven Poiseuille flow and shear flow factor $\phi_S$ represents added shear flow caused by asperity [15,16]. Also, contact flow factor $\phi_C$ and roughness flow factor $\phi_R$ are used to relate averaged film thickness with local film thickness for compressible flow [14,17]. Those flow factors can be pre-calculated for nondimensional film thicknesses assuming Gaussian and isotropic surface roughness, and the results can be found in [14].

$$\nabla\cdot\left(\phi_P\left(\frac{Kh^3}{12\mu}\nabla\rho\right)\right)=\nabla\cdot\left(\rho v_m\left(\phi_R R_q+\phi_C h\right)\right)+$$
$$\nabla\cdot\left(\rho\phi_S R_q\left(\frac{\vec{v}_t-\vec{v}_b}{2}\right)\right)+\frac{\partial\rho\left(\phi_R R_q+\phi_C h\right)}{\partial t}\qquad(4)$$

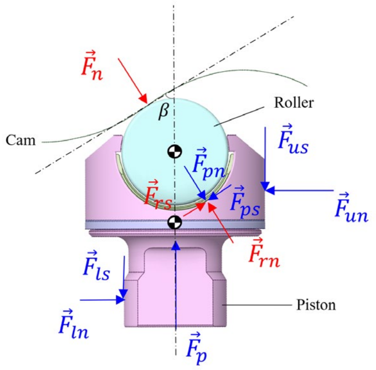


*Figure 5: Free body diagram for roller and piston.*

### 2.3 Asperity contact

In mixed or boundary lubrication regimes, the asperity contact pressure provides additional load support for a lubricating interface. Lee et al [18] provided the curve-fitted analytic model that can predict averaged asperity contact pressure for given material properties and fluid film thickness, considering the elastic and plastic behavior of surfaces (eq. (5)). The surface roughness was measured for all lubricating surfaces, and the equivalent surface roughness were used for eq. (5) and flow factor calculations for each lubricating interface. In addition, the measured surface profile of the roller from partial crowning which is known to prevent high stress at the edges was implemented to provide an additional gap height to the edges.

$$\ln\left(\frac{\bar{h}}{R_q}\right)=\sum_i\left(\vec{r}_G^T G_i\vec{H}\right)\bar{P}^i\qquad(5)$$

### 2.4 Kinematics and rigid body dynamics

As shown in fig. 4, the rotational velocity of the roller can be obtained by assuming no slip at the contact point, which means the velocity at the contact point should be zero (eq. (6)). The calculated rotational velocity was imported as a look-up table which is a function of a cylinder block rotation angle.

$$\vec{V}_c=\vec{V}_r+\vec{\omega}_r\times\left(\vec{R}_c-\vec{R}\right)=\mathbf{0}\qquad(6)$$

The free-body diagram for the piston and roller is shown in fig. 5. The forces applied to the roller are represented in red and the forces applied to the piston are represented in blue. The pressure force $\vec{F}_p$ is calculated from the piston chamber pressure in the LP model. The normal force $\vec{F}_n$ represents the reaction force from the contact point and can be approximated from force balance using contact angle $\beta$ without considering friction from the piston-cylinder interfaces. $\vec{F}_{rs}$ and $\vec{F}_{rn}$, are shear and normal force applied to the roller by the roller – bushing interface, and $\vec{F}_{ps}$ and $\vec{F}_{pn}$ are shear and normal force applied to the piston by the same lubricating interface. Similarly, $\vec{F}_{us}$ and $\vec{F}_{un}$ are shear and normal force applied to the piston by upper piston – cylinder lubricating interface, and $\vec{F}_{ls}$ and $\vec{F}_{ln}$ are shear and normal force applied to the piston by the lower piston – cylinder lubricating interfaces. Also, the cylinder block was set to rotate at a constant shaft speed. Since the motion in axial direction is constrained by a thrust bearing and the valving interface, only planar motions were considered for the roller and piston with Newton's second law (eq. (7,8)).

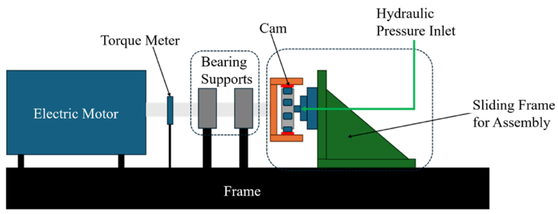


*Figure 6: Schematic diagram for experimental setup.*

$$\Sigma\vec{F}=\frac{d}{dt}\vec{P}\qquad(7)$$
$$\Sigma\vec{M}=\frac{d}{dt}\vec{L}\qquad(8)$$

### 2.5 Solid deformation

In general, deformation considerably affects hydrodynamic pressure and film thickness distribution in an elastohydrodynamic lubrication. Moreover, the roller – bushing interface and the piston – cylinder interface have a mutual effect on the overall deformation of the piston. One of the most successful methods to consider deformation for a Reynolds equation is the influence matrix method [19]. By solving a linear static elastic equation offline using a finite element method, the relationship between the deformation gap $h_{def,i}$ for i-node and reference pressure $p_{ref}$ on j-face in fluid film domains is found in matrix $[IM]_{i,j}$ as eq. (9). Then, the matrix operation is performed in the main coupled simulation for combined pressure $p_j$ which includes hydrostatic, hydrodynamic, and contact pressure for j-face in fluid films. To generate the influence matrix for each solid body, the mechanical properties of standard alloy steel were used for the roller, piston, and cylinder block, and the equivalent mechanical property was used for PEEK-based bushing.

$$h_{def,i}=[IM]_{i,j}\left(p_j/p_{ref}\right)\qquad(9)$$

## 3 Experimental Validation

### 3.1 Experimental setup

The friction torque from the simulated lubricating interfaces was compared to measurement using an experimental setup with a torque meter (fig. 6). To isolate frictions from other sources of power loss, the electric motor

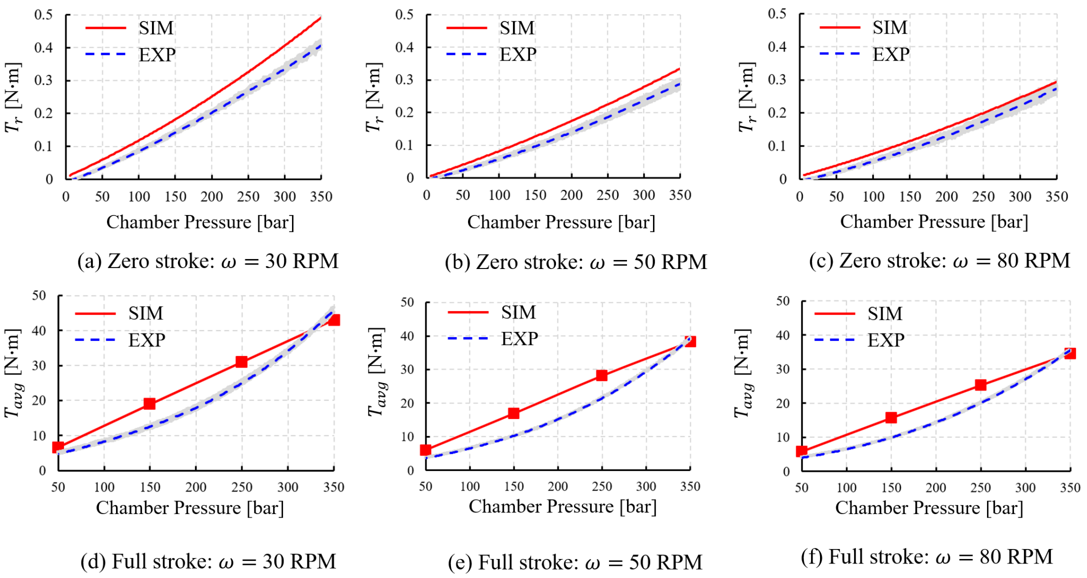


*Figure 7: Friction torque comparisons.*

rotates the cam through a shaft supported by two bearing supports while pressurized fluid is supplied to the inlet of the fixed cylinder block. During the measurement, the chamber pressure was controlled to increase slowly. This experimental setup is different from actual motor operating conditions where cylinder block ports are alternatively connected to valve block ports and pressurization and depressurization of chamber pressure occur. Additionally, ISO VG46 was used as the working fluid, and the inlet temperature of the cylinder block was controlled to 50 °C by an external cooling system. For all measurements, the torque meter was calibrated to eliminate the friction torque from the bearing supports, and the chamber pressure was monitored.

### 3.2 Friction torque comparison

First, a zero-stroke cam without a wavy profile was used to prevent reciprocating motion of the piston where only friction from the roller – bushing interface was measured. The measurement inevitably includes the friction from roller – cam interface, but the amount may be negligible when assuming pure rolling. The measured friction torque $T_s$ from the shaft can be related to simulated roller friction torque $T_r$ using eq. (10, 11) where $P$, $N$, $\omega_s$, and $\omega_r$ represent the power loss, number of rollers, shaft speed, roller speed, and $D_c$ and $D_r$ represent the diameter of the cam and roller. Similar to the experiment, the inlet pressure and resultant force applied were increased gradually for different shaft speeds during the simulation. The measurement and simulation results showed a relatively good match in trends (fig. 7 (a, b, c)) although the growing deviation can be observed for high chamber pressure at 30 RPM, which can be attributed to nonlinear asperity contact behavior at this condition.

$$P = T_s \omega_s = N T_r \omega_r \tag{10}$$

$$\omega_r = (D_c / D_r) \omega_s \tag{11}$$

Second, the full-stroke cam with a wavy profile was used to measure the friction from all lubricating interfaces including the roller – bushing interface and piston – cylinder interfaces. Unlike the case for the zero-stroke cam with the gradual pressure increase, the simulation was run for 12 operating conditions due to high computational cost. Averaged friction torque over a period of the reciprocating motion of the piston is shown in fig. 7 (d, e, f). The power loss from the piston – cylinder interfaces was much greater than that from the roller – bushing interface and mostly due to asperity contact friction. The simulation results only matched well with the measurement for specific conditions, indicating different trends in the friction torque with increasing chamber pressure. Experimental results suggested apparently quadratically increasing frictional torque while the friction torque from the simulation linearly increased.

## 4 Results and discussion

Unlike the experimental set up where the chamber pressure is slowly increased or maintained, the simulation results in this section considers transient chamber pressure and valving port timing by solving the lumped parameter model.

### 4.1 Roller – bushing interface

The fluid films are strongly coupled through dynamics and deformation and this coupling significantly affects

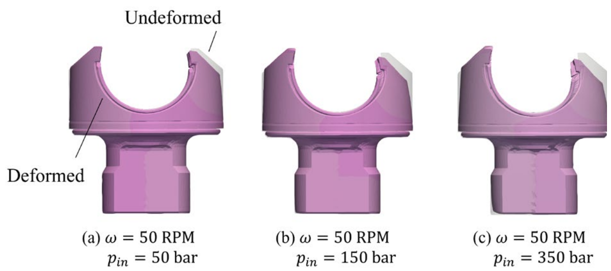


*Figure 8: Deformation of piston (exaggerated).*

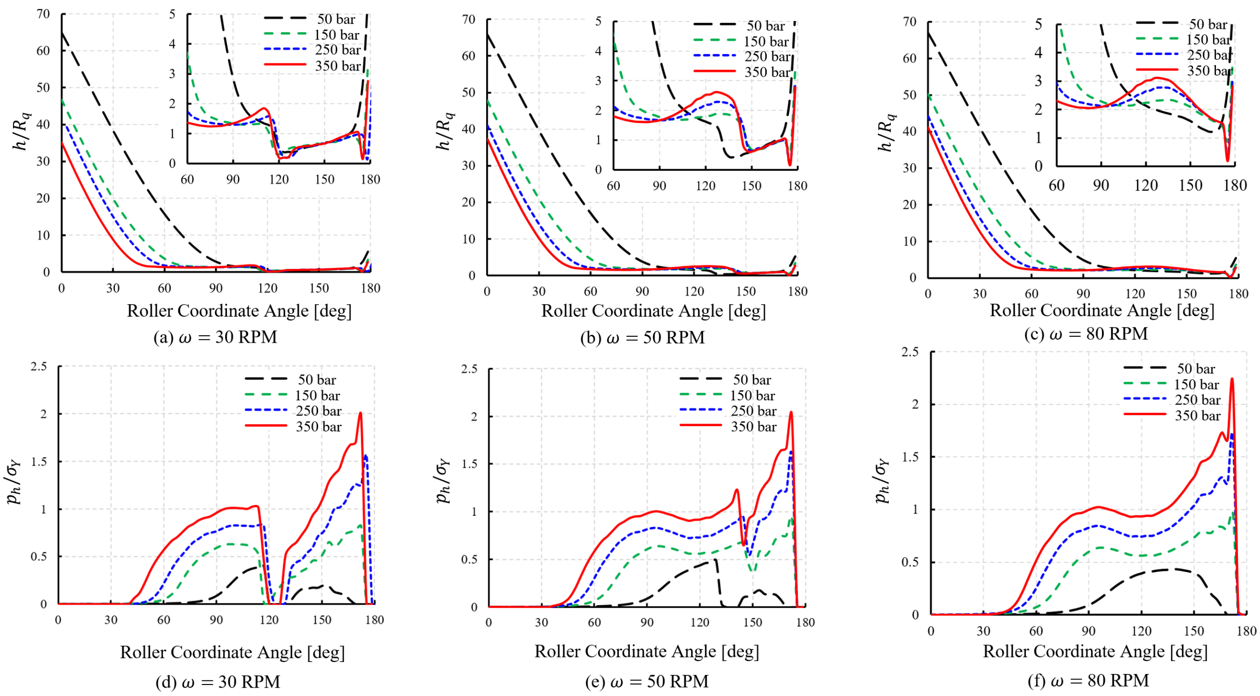


*Figure 9: Roller – bushing interface results at the midplane.*

hydrodynamic and asperity contact pressures and fluid film thickness distribution. This is especially important when the contact angle $\beta$ is at the maximum and the piston exerts a maximum force on the cylinder wall, and as a result, the piston deforms asymmetrically (fig. 8). The hydrodynamic pressure and film thickness distribution of the roller – bushing interface at this moment are shown in fig. (9, 10). In fig. (9), the x-axis represents the roller coordinate angle at the mid-plane of the interface, and the y-axis represents the corresponding dimensionless hydrodynamic pressure and film thickness. When the radial piston motor is under low-duty operating conditions such as inlet pressure of 50 bar and shaft speed of 80 RPM, the minimum dimensionless film thickness is greater than 1, indicating a partial lubrication regime [20]. However, for all shaft speeds with the inlet pressure of 150, 250, and 350 bar, the asymmetric deformation of the piston bore reduced the film thickness significantly near the edge (180°), involving the hydrodynamic pressure peak and asperity contact. This behavior matched well with the experimental observation made in the previous study by Nilsson et al [5] which demonstrated severe wear near the edge. Moreover, when the shaft speed decreased from 80 RPM to 50 RPM, the loss of hydrodynamic pressure induced more asperity contact before the roller coordinate angle of 150° (fig. 9 (e) and fig. 10 (b, e)). This behavior is even more pronounced when the shaft speed is 30 RPM, showing a complete loss of hydrodynamic pressure around 120° for all inlet pressure conditions (fig. 9 (d) and fig. 10 (a,d)). The film thickness remained relatively constant due to the severe solid contact, and this eliminated the primary hydrodynamic pressure build-up mechanism, physical wedge from the geometrical nominal clearance. These results demonstrated the tribological behavior of the roller – bushing interface is highly sensitive to the operating conditions, and

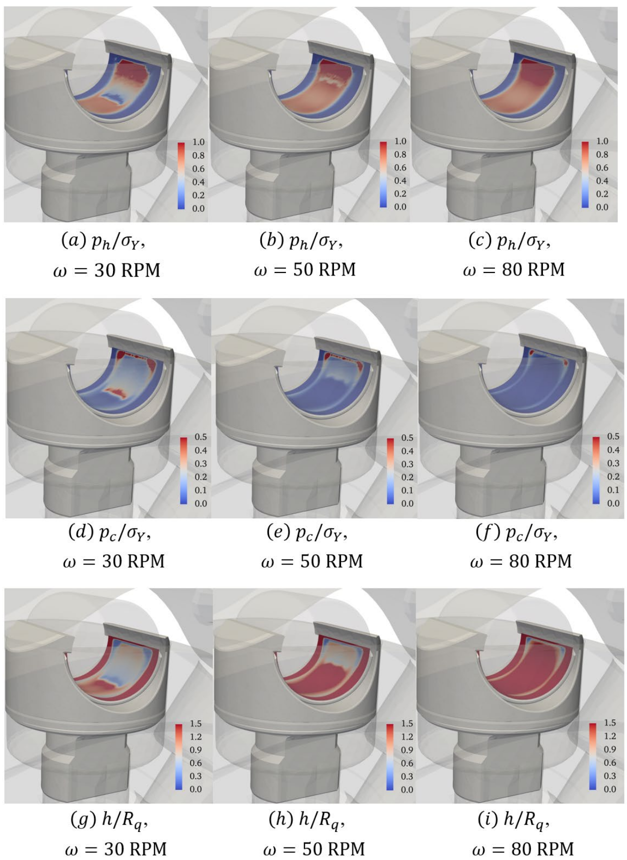


*Figure 10: Roller – bushing interface for $p_{in} = 250\ bar$.*

high loading and low shaft speed can pose wear or seizure as observed in [5].

### 4.2 Piston – cylinder interface

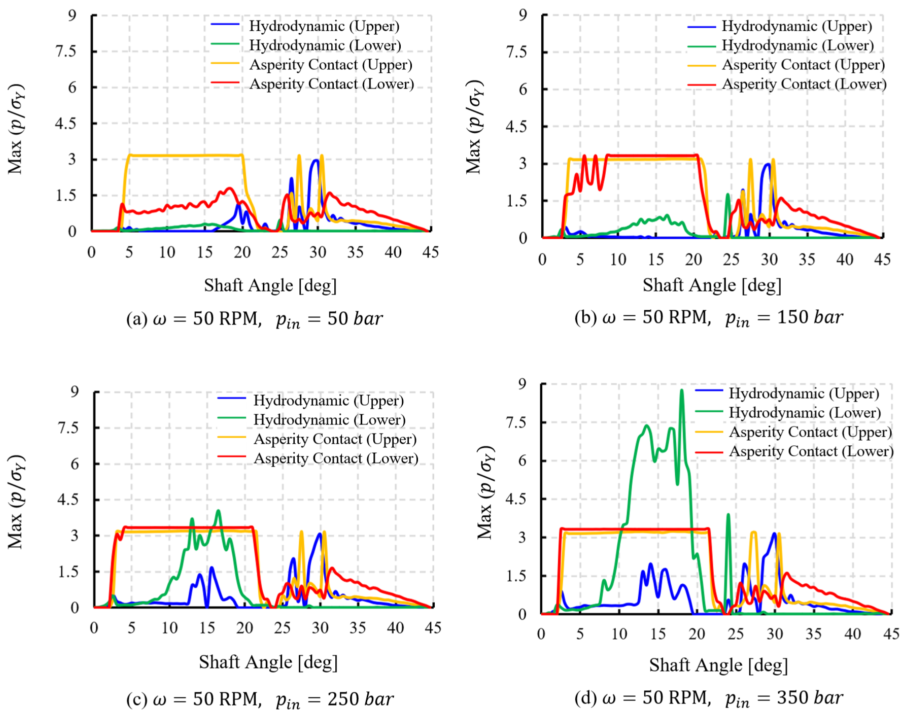


(a) $\omega = 50$ RPM, $p_{in} = 50\ bar$ (b) $\omega = 50$ RPM, $p_{in} = 150\ bar$

(c) $\omega = 50$ RPM, $p_{in} = 250\ bar$ (d) $\omega = 50$ RPM, $p_{in} = 350\ bar$

*Figure 11: Maximum dimensionless hydrodynamic and contact pressure.*

When the contact angle is not zero, the geometrical nominal clearance between a piston and cylinder bore can induce tilting of the piston which can largely influence the hydrodynamic and contact pressure distribution on the piston – cylinder interfaces. To investigate those behaviors, the maximum value of hydrodynamic and asperity contact pressures over each interface domain for a period of reciprocating motion are shown for the shaft speed of 50 RPM with different inlet pressures (fig. 11). From 0° to 22.5° shaft angle, the piston chamber is connected to a high-pressure inlet, and the piston starts to move upward, tilting in the clockwise direction. This tilting of the piston offers a physical wedge only for the lower lubricating films, and the upper fluid film should rely on squeeze motion to build up hydrodynamic pressure. Therefore, the asperity contact pressure of the upper fluid film rapidly increased to hardness value and supported most of the loading for all inlet pressure conditions (fig. 12 (d, e, f)). It should be noted that the hydrodynamic pressure only temporarily existed up to the shaft angle of 13° due to increased squeeze motion, and the pressure spikes from the shaft angle of 13° to 22.5° originated from a few isolated cells which cannot contribute much to the load support (fig. 12 (c)). On the other hand, the lower fluid films can build up hydrodynamic pressure from the physical wedge, showing a significant increase in the high loading (fig. 11 (d) and fig. 12 (c)). However, the asperity contacts also occurred for lower films because the hydrodynamic alone cannot support the loading, and this asperity contact is highly dependent on the loading (fig. 12 (d, e, f)). When the piston chamber is connected to the low-pressure outlet of 20 bar which corresponds to 22.5° to 45° shaft angle, the piston moves downward. The counterclockwise tilting of the piston provides the physical wedge only to the upper fluid film. Therefore, the maximum

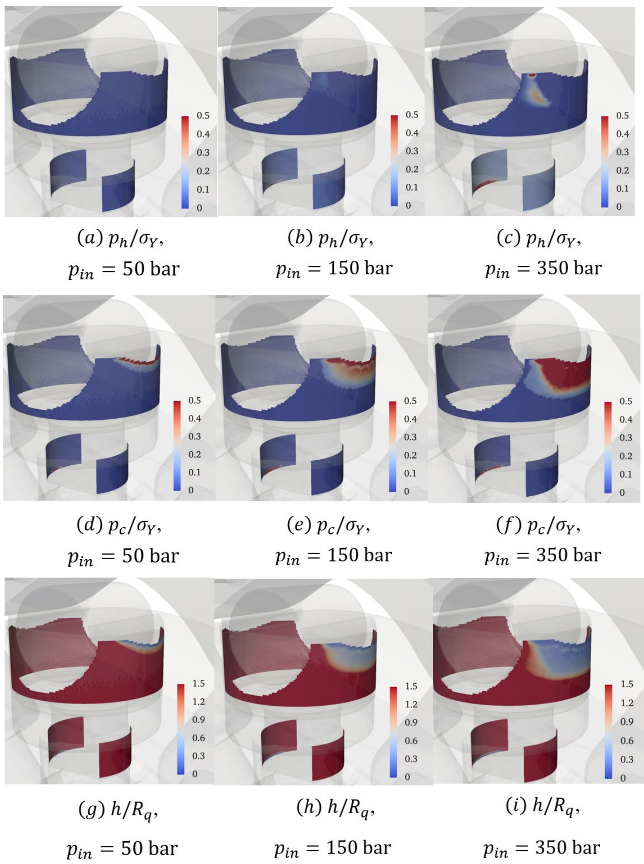


(a) $p_h/\sigma_Y$, $p_{in} = 50$ bar (b) $p_h/\sigma_Y$, $p_{in} = 150$ bar (c) $p_h/\sigma_Y$, $p_{in} = 350$ bar

(d) $p_c/\sigma_Y$, $p_{in} = 50$ bar (e) $p_c/\sigma_Y$, $p_{in} = 150$ bar (f) $p_c/\sigma_Y$, $p_{in} = 350$ bar

(g) $h/R_q$, $p_{in} = 50$ bar (h) $h/R_q$, $p_{in} = 150$ bar (i) $h/R_q$, $p_{in} = 350$ bar

*Figure 12: Piston – cylinder interface for $\omega = 50\ RPM$*

hydrodynamic pressure of the upper fluid film was higher when the piston moved downward than when the piston moved upward despite the much smaller loading. On the other hand, the lower fluid films cannot build up hydrodynamics pressure,

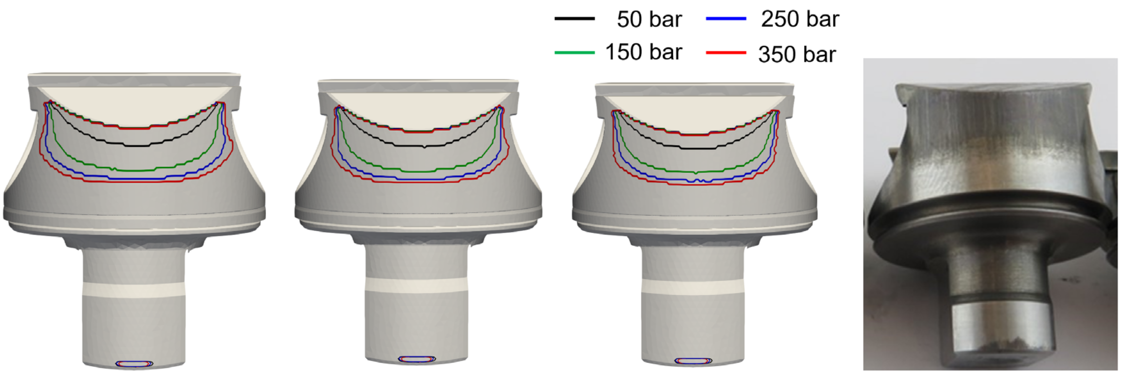


(a) $\omega$ = 30 RPM (b) $\omega$ = 50 RPM (c) $\omega$ = 80 RPM (d) Piston Wear

*Figure 13: Asperity contact area.*

and most of the loading is supported by asperity contact pressure. The region of high asperity contact pressure (>100 bar) during the reciprocating motion is illustrated in fig. 13 (a, b, c) for various shaft speed and inlet pressure conditions. The predicted area was compared to the wear area of a piston under real motor operating conditions and showed a good match in the location.

In terms of the power loss calculation for the piston – cylinder interfaces, the viscous friction was almost negligible compared to asperity contact friction. Also, it should be noted that the difference in trends between the simulation and measurement as shown in fig. 7 is based on the constant solid friction coefficient used in the simulation model. However, the experimental results demonstrated an increasing friction coefficient, observed in a typical Stribeck curve where the friction coefficient increases when the lubrication regime changes from mixed lubrication to boundary lubrication.

### 4.3 Power loss analysis

The ratio of power loss to theoretical power $P/P_{th}$ (eq. 12) was calculated to identify power loss contributions as shown in fig. 14.

$$P/P_{th} = P/(\Delta p \cdot V_{disp} \cdot \omega_s) \tag{12}$$

The power loss from the upper fluid film accounts for more than 45 % to 70 % of the total power loss depending on operating conditions. This result is expected from the above discussion that the upper fluid film is subject to severe asperity contact. When the inlet pressure increased from 50 bar to 150 bar, the increased hydrodynamic pressure from squeeze motion decreased the power loss ratio. Also, the lower fluid films demonstrated negligible power loss ratio in most cases because they can build up hydrodynamic pressure during the upstroke and are subject to a much lower load than the upper fluid film. The power loss ratio from the roller — bushing interfaces is relatively small because it can always build up hydrodynamic pressure to a certain degree, and benefit from the low solid friction coefficient of the PEEK-based bushing to steel interface. Besides the lubricating fluid film, the developed model can predict the power loss from the orifice and port from the LP model. Those additional losses represent the pressure drop of the flow caused by viscous dissipation, occurring at connections in the cylinder block. The port loss ratio was almost negligible for most of the cases considered while it showed a maximum value of 1 percent in low inlet pressure of 50 bar and high shaft speed of 80 RPM condition. The throttling loss represented as an orifice, however, strongly depended on the inlet pressure and shaft speed. When the inlet pressure changed from 50 bar to 150 bar, the throttling power loss ratio decreased for all shaft speeds. This may be because the small pressure difference between the inlet and piston chamber might lead to the incomplete filling of the piston chamber, increasing the duration of the pressure drop. However, as the inlet pressure increased from 150 bar to 250 bar and 350 bar, the throttling loss ratio increased. If the pressure inlet is high enough to avoid incomplete filing, the additional pressure increase can contribute to higher flow velocity across the orifice area which induces higher viscous dissipation.

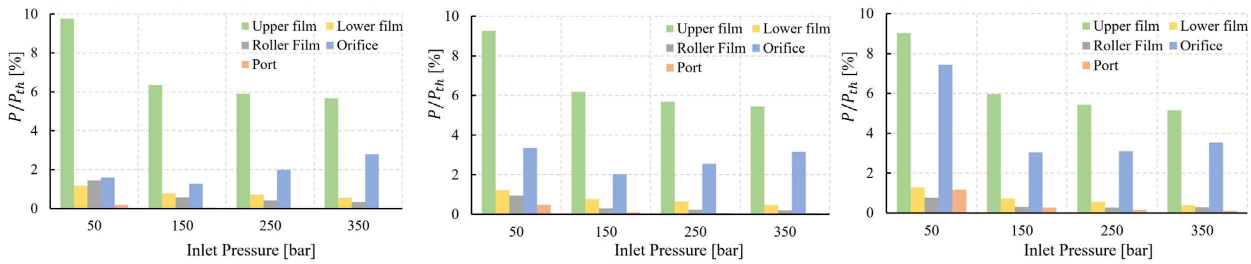


(a) $\omega$ = 30 RPM (b) $\omega$ = 50 RPM (c) $\omega$ = 80 RPM

*Figure 14: Power loss analysis.*

## 5 Conclusion and outlook

A novel simulation method was developed to investigate the piston lubricating interfaces in a radial piston motor. The simulation model can account for the lumped parameter model, body dynamics, fluid films, asperity contact, and deformation in a fully coupled way. The consideration of those multiphysics was found to be essential in determining tribological behaviors of the lubricating interfaces. The power loss analysis was conducted for all lubricating interfaces and hydraulic components in the lumped parameter model. The upper piston — cylinder interface was a major contributor, followed by the throttling (orifice) loss for all operating conditions considered. In summary, the developed model can be used to access the design parameters including the nominal clearance, piston geometry, cam profile, and valving port area and timing. Also, the model can provide insights into the lubricating behavior of the fluid films around a piston in a radial piston motor.

As a next step, a more realistic model for the solid friction coefficient needs to be developed because the current model overpredicts the friction torque from piston — cylinder interface for the medium inlet pressure range. Even though the new model may allow more accurate friction torque and power loss calculations, the effect of solid friction coefficient on other physical quantities, such as hydrodynamic and asperity contact pressures, and film thickness distribution in the lubricating interfaces may be minimal. Since the friction forces are relatively small compared to the hydrostatic force on the piston or the normal force on the roller, a similar body dynamic will be applied, and the current results for tribological behaviors would still be valid.

## Nomenclature

| Designation | Denotation | Unit |
|---|---|---|
| $\rho$ | Density of a working fluid | $kg/m^3$ |
| $\mu$ | Viscosity of a working fluid | $Pa \cdot s$ |
| $\kappa$ | Minor loss coefficient | $-$ |
| $v$ | Flow velocity magnitude | $m/s$ |
| $t$ | Time | $s$ |
| $p$ | Pressure | $Pa$ |
| $f$ | Darcy friction factor | $-$ |
| $V$ | Piston chamber volume | $m^3$ |
| $Q$ | Volume flow rate | $m^3/s$ |
| $P$ | Power loss | $W$ |
| $N$ | Number of rollers | $-$ |
| $L$ | Port length | $m$ |
| $D$ | Port diameter | $m$ |
| $A$ | Orifice Area | $m^2$ |
| $\mathrm{K}$ | Bulk viscosity | $Pa$ |
| $h$ | Local fluid film thickness | $m$ |
| $\phi_S$ | Shear flow factor | $-$ |
| $\phi_R$ | Roughness flow factor | $-$ |
| $\phi_P$ | Pressure flow factor | $-$ |
| $\phi_C$ | Contact flow factor | $-$ |
| $\omega_s$ | Shaft speed | $rad/s$ |
| $\omega_r$ | Roller angular speed | $rad/s$ |
| $\sigma_Y$ | Minimum yield strength of two surfaces | $Pa$ |
| $v_m$ | Mean velocity of two surfaces | $m/s$ |
| $p_{ref}$ | Reference pressure | $Pa$ |
| $p_j$ | Pressure on j$^{th}$ face | $Pa$ |
| $p_{in}$ | Inlet pressure | $Pa$ |
| $p_h$ | Hydrodynamic pressure | $Pa$ |
| $V_{disp}$ | Piston displacement per shaft revolution | $m^3$ |
| $T_r$ | Friction torque of a roller | $N \cdot m$ |
| $R_q$ | Equivalent surface roughness | $m$ |
| $\vec{R}$ | Roller position | $m$ |
| $\vec{P}$ | Linear momentum | $kg \cdot m/s$ |
| $\vec{M}$ | Moment | $N \cdot m$ |
| $\vec{L}$ | Angular momentum | $kg \cdot m^2/s$ |
| $\vec{H}$ | Hardness parameter | $-$ |
| $\vec{F}$ | Force | $N$ |
| $D_r$ | Roller dimeter | $m$ |
| $D_c$ | Cam diameter | $m$ |
| $C_f$ | Orifice discharge coefficient | $-$ |
| $h_{def,i}$ | Deformation gap of i$^{th}$ node | $m$ |
| $\bar{h}$ | Averaged fluid film thickness | $m$ |
| $\vec{\omega}_r$ | Roller angular velocity | $rad/s$ |
| $\vec{v}_v$ | Bottom surface velocity | $m/s$ |
| $\vec{v}_t$ | Top surface velocity | $m/s$ |
| $\vec{r}_G^T$ | Isotropic index parameter | $-$ |
| $\vec{V}_r$ | Roller velocity | $m/s$ |
| $\vec{V}_c$ | Contact point velocity | $m/s$ |
| $\vec{R}_c$ | Contact position | $m$ |
| $\bar{P}^i$ | Contact pressure polynomial | $-$ |
| $[IM]_{i,j}$ | Influence matrix | $-$ |

## References


[1] H. Olsson, J. Ukonsaari, Wear testing and specification of hydraulic fluid in industrial applications, *Tribology International*, 36(11): 835-841, 2003.

[2] C. Zhang, H. Tan, Y. Fang, X. Zhang, Y. Yang, Y. Duan, M. Han, S. Cui, B. Xu, J. Zhang, Deformation pre-compensated optimization design of cam ring for low pulsation hydraulic motors, *Journal of Zhejiang University SCIENCE A* , 24(2) 130–145, 2023.

[3] U. Pettersson, S. Jacobson, Textured surfaces for improved lubrication at high pressure and low sliding speed of roller/piston in hydraulic motors, *Tribology International*, 40(2): 355-359, 2007.

[4] R. Lewis, Friction in a hydraulic motor piston/cam roller contact lined with PTFE impregnated cloth, *Wear,* 266(7–8): 888-892, 2009.

[5] D. Nilsson, B. Prakash, Investigation into the seizure of hydraulic motors, *Tribology International,* 43(1–2): 92-99, 2010.

[6] L. Dahlén , H. Olsson, Analysis of two sliding contacts inside a radial piston hydraulic motor, *Proceedings of the JFPS International Symposium on Fluid Power 2002*, (5-2): 537-542, 2002.

[7] P. Isaksson, D. Nilsson, R. Larsson, Elasto-hydrodynamic simulation of complex geometries in hydraulic motors, *Tribology International*, 42(10): 1418-1423, 2009.

[8] P. Isaksson, D. Nilsson, R. Larsson, and A. Almqvist, The influence of surface roughness on friction in a flexible hybrid bearing, *Proceedings of the Institution of Mechanical Engineers, Part J: Journal of Engineering Tribology*, 225(10):975-985, 2011.

[9] X. Zhang, J. Zhang, B. Xu, Z. Yang, Q. Zhao, H. Zhang, The effect of slotted hole on minimum oil film thickness of piston in radial piston hydraulic motor, *Proceedings of the ASME/BATH 2021 Symposium on Fluid Power and Motion Control*, 2021.

[10] C. Zhang, X. Zhang, P. Dong, H. Zhang, Z. Zheng, J. Zhang, B. Xu, Composite thermal oil film lubrication model for hybrid journal bearings, *Tribology International* 194, 2024.

[11] C. Li, T. Jiang, C. Liu, H. Xu, G. Shi, Investigation of the leakage in the flow distribution pair of radial piston hydraulic motors through CFD analysis and experiments, *Flow Measurement and Instrumentation*, 96, 2024.

[12] T. Ransegnola, L. Shang, Andrea Vacca, A study of piston and slipper spin in swashplate type axial piston machines, *Tribology International*, 167, 2022.

[13] S. Mukherjee, L. Shang, A. Vacca, Numerical analysis and experimental validation of the coupled thermal effects in swashplate type axial piston machines, *Mechanical Systems and Signal Processing*, 220, 2024.

[14] T. Ransegnola, A strongly coupled simulation model of positive displacement machines for design and optimization, Doctoral Thesis, Purdue University, 2020.

[15] N. Patir and H. S. Cheng, An average flow model for determining effects of three-dimensional roughness on partial hydrodynamic lubrication, *Journal of Tribology*, 100(1): 12-17, 1978.

[16] N. Patir and H. S. Cheng, Application of Average Flow Model to Lubrication Between Rough Sliding Surfaces, *Journal of Tribology*, 101(2):220-229, 1979.

[17] W. Chengwei and Z. Linqing, An average Reynolds equation for partial film lubrication with contact factor," *Journal of Tribology*, 111(1):188-191, 1989.

[18] Si C. Lee and N. Ren, Behavior of elastic-plastic rough surface contact as affected by surface topography, load, and material hardness, *Tribology Transactions*, 39(1):67-74, 1996.

[19] M. Pelosi, M. Ivantysynova, The impact of axial piston machines mechanical parts constrain conditions on the thermo-elastohydrodynamic lubrication analysis of the fluid film interfaces, Internation Journal of Fluid Power, 14(3):35-51, 2013.

[20] B.J Hamrock, S.R. Schmid, & B.O. Jacobson, Fundamentals of Fluid Film Lubrication (2nd ed.). CRC Press. 2004.